

Journal of Biomedical Optics

SPIEDigitalLibrary.org/jbo

Reduction of image artifacts in three-dimensional optical coherence tomography of skin *in vivo*

Yih Miin Liew
Robert A. McLaughlin
Fiona M. Wood
David D. Sampson

Reduction of image artifacts in three-dimensional optical coherence tomography of skin *in vivo*

Yih Miin Liew,^a Robert A. McLaughlin,^a Fiona M. Wood,^{b,c} and David D. Sampson^{a,d}

^aThe University of Western Australia, School of Electrical, Electronic & Computer Engineering, Optical + Biomedical Engineering Laboratory, M018, 35 Stirling Highway, Crawley WA 6009, Australia

^bRoyal Perth Hospital, Burns Service of Western Australia, Wellington Street, Perth WA 6000, Australia

^cThe University of Western Australia, School of Surgery, Burn Injury Research Unit, 35 Stirling Highway, Crawley WA 6009, Australia

^dThe University of Western Australia, Centre for Microscopy, Characterisation & Analysis, M010, 35 Stirling Highway, Crawley, Perth, WA 6009, Australia

Abstract. This paper presents results of *in vivo* studies on the effect of refractive index-matching media on image artifacts in optical coherence tomography (OCT) images of human skin. These artifacts present as streaks of artificially low backscatter and displacement or distortion of features. They are primarily caused by refraction and scattering of the OCT light beam at the skin surface. The impact of the application of glycerol and ultrasound gel is assessed on both novel skin-mimicking phantoms and *in vivo* human skin, including assessment of the epidermal thickening caused by the media. Based on our findings, recommendations are given for optimal OCT imaging of skin *in vivo*. © 2011 Society of Photo-Optical Instrumentation Engineers (SPIE). [DOI: 10.1117/1.3652710]

Keywords: optical coherence tomography; OCT; skin; *in vivo* imaging; image artifacts; refractive-index matching; epidermal swelling; artifact reduction.

Paper 11228R received May 9, 2011; revised manuscript received Sep. 9, 2011; accepted for publication Sep. 23, 2011; published online Nov. 3, 2011.

1 Introduction

Optical coherence tomography¹ (OCT) is a high-resolution imaging modality appropriate for assessment of skin *in vivo*. Structures such as the stratum corneum, epidermis, dermo-epidermal junction, blood vessels, and skin appendages, such as hair follicles, sweat ducts, and sebaceous glands, have been identified using OCT and good correlations with histology have been published.^{2,3} OCT has been shown to provide an accurate measure of epidermal thickness validated against cryostat histology,⁴ and studies have used OCT to monitor epidermal thickness changes due to UV radiation,^{5,6} aging,⁷ and skin diseases.⁸ OCT has also been applied to real-time assessment of skin inflammatory disease⁸⁻¹³ and tumors,¹⁴⁻¹⁶ the examination of skin vasculature dilation,¹⁷ and the efficacy of laser treatment of such vascular malformations as port-wine stain birthmarks.³

OCT imaging of skin can suffer from significant image artifacts. We consider an image artifact to be any image feature not indicative of a structure in the skin. Image artifacts may present as extraneous, non-existent visual features, or distortions (in shape or intensity). The presence of artifacts produces an inaccurate representation of the underlying skin morphology and complicates the clinical interpretation of the images. Several types of instrument- and sample-induced artifacts have been reported to date for OCT. Instrument-induced artifacts include those due to conjugate image features (or mirror artifact),¹⁸ optical aberration (or fan distortions),¹⁹ and autocorrelation.²⁰

Sample-induced artifacts include those due to horizontal banding (or birefringence artifact),²¹ shadowing,²² refraction,²³ and motion.²⁴ In this study, we have classified two prominent types of a sample-induced artifact in OCT images of skin, which we shall refer to as intensity distortion and morphological distortion. These artifacts are present particularly when the system is used in noncontact mode (i.e., when an air-gap exists between the skin and the focusing optics of the OCT scanner).

Intensity distortions appear as vertical streaks of low-intensity backscatter under skin furrows, which are grooves of variable depth on the skin surface (Fig. 1). The low-intensity streaks are observed to correlate with the location of the surface furrows and broaden with depth. We expect that they are associated with refraction and divergence of the light beam caused by the skin's furrowed surface and the associated abrupt change in refractive index (RI) between the skin and air. These low-intensity streaks cause an imprint of the skin surface topography to appear at all depths of the OCT scan. In *en face* images (i.e., lateral cross-sectional images) under the skin surface, this imprint creates extraneous features, presenting as lines aligned to the surface furrows.

Two types of morphological distortion are observed. One type occurs because OCT systems generate images based on optical path length, instead of the true physical path length. As optical path length is a function of the RI of the medium, different amounts of air and tissue traversed in reaching a feature will change the optical path length to the feature. Thus, the surface shape and thickness of the overlying tissue can modify the apparent depth of a feature. In the other type of distortion, features are displaced laterally because the surface shape and refraction

Address all correspondence to: Yih Miin Liew, Optical + Biomedical Engineering Laboratory, School of Electrical, Electronic & Computer Engineering, University of Western Australia, M018, 35 Stirling Highway, Crawley WA 6009, Australia; Tel: +61 8 6488 3916; Fax: +61 8 6488 1319; E-mail: liewy08@student.uwa.edu.au.

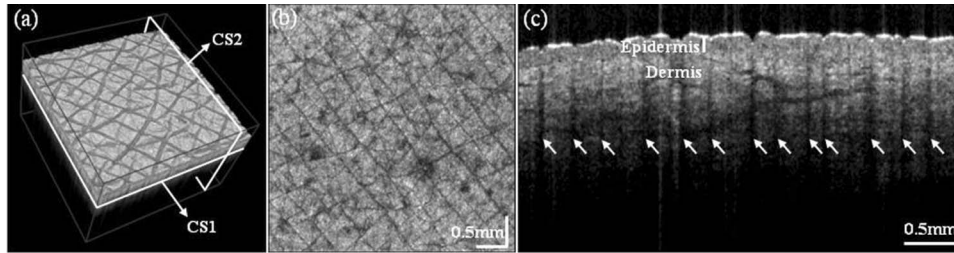


Fig. 1 OCT images of the skin of the medial calf of a human subject illustrating intensity distortion artifact: (a) 3D solid rendering of the skin showing skin surface topography. The labeled cross-sectional images are shown in (b) and (c); (b) *En face* image (CS1) at 400- μm depth (uncorrected for RI) below the surface showing evidence of artifactual lines replicating skin surface topography; (c) vertical cross-sectional images (CS2) highlighting the source of the artifact: low-intensity, vertical streaks (indicated by arrows) which emerge at multiple locations directly under the skin furrows. Vertical scale bar in (c) is not corrected for RI.

affect the angle at which the OCT light beam propagates beneath the tissue surface.

Such artifacts have been observed in images in previously published papers, but have not been specifically studied.^{8,10,25–28} Some researchers have used glycerol and ultrasound gel to reduce RI mismatch and to improve image quality.^{2,5,9,11,29–31} The efficacy of these media in reducing image artifacts has not previously been assessed. In addition, the application of glycerol or ultrasound gel is known to affect the thickness of the skin but such effects on the epidermis have not previously been examined in detail.

In this study, we investigate and assess the efficacy of glycerol and ultrasound gel in reducing OCT image artifacts. Experiments were carried out on both novel skin mimicking-phantoms and on *in vivo* human skin. We also assessed the effect of these media on epidermal thickness, a common parameter in the assessment of skin. Based on our findings, recommendations are given for optimal OCT imaging of skin *in vivo*.

2 Methods

2.1 OCT System

A fiber-based, swept-source frequency-domain OCT system (OCS1300SS, Thorlabs, USA), comprising of a broadband, swept laser source and a Michelson interferometer with balanced detection, was used in this study. The laser source has a central wavelength of 1325 nm and a full-width at half-maximum bandwidth of 100 nm. The average optical power of the probing beam incident on the sample was 4.7 mW and the axial A-scan frequency was 16 kHz. The system has a manufacturer-specified axial resolution of 12 μm in free space corresponding to ~ 8.4 μm in skin (assuming a skin RI of 1.43, Ref. 27). The B-scan (set of 800 A-scans) frequency was 15.4 frames/s and the three-dimensional (3D) acquisition time was 55 s. All images acquired were $4 \times 4 \times 3$ mm ($x \times y \times z$) in size and consisted of $800 \times 800 \times 512$ pixels.

The sample arm was configured as a handheld probe. An adjustable spacer was affixed to the probe (Fig. 2) to maintain a constant distance between the objective lens and the sample. A glass cover slip was attached to the bottom of the spacer to act as a window for imaging. The working distance and numerical aperture of the objective lens is 25.1 mm and 0.056, respectively, yielding a specified diffraction-limited lateral system resolution of 15 μm .

2.2 Experimental Design

2.2.1 Skin phantom study

A disk-shaped silicone phantom was designed to investigate the intensity artifact. Its entire surface (1.4-cm diameter) was cast into a positive replica of human ventral forearm skin from a negative imprint produced by melted wax impressed on the skin. To mimic the scattering properties of tissue, 0.3% weight of titanium dioxide (powder, particle size < 5 μm , Sigma-Aldrich, St Louis, Missouri, USA) per weight of silicone (Elastosil® RT 601 A/B, Wacker, Munich, Germany) were introduced as scatterers. The mixture was mechanically stirred for 30 to 45 min to disperse the scatterers homogeneously and placed under vacuum to remove air bubbles. The curing agent was added (in the ratio to silicone of 1:9) and the mixture was stirred gently (to avoid further incorporation of air bubbles) for 30 s before being poured into a mold, capped with the wax skin imprint, and cured for 24 h resulting in a final thickness of 4 ± 0.1 mm. We refer to this phantom as the intensity phantom.

A second silicone/titanium dioxide phantom was designed to investigate the morphological artifact. It is identical to the first phantom, except that only half of its surface was cast into a positive skin replica, and a series of single-mode optical fibers (Corning, SMF-28, 125- μm diameter, coating removed) were

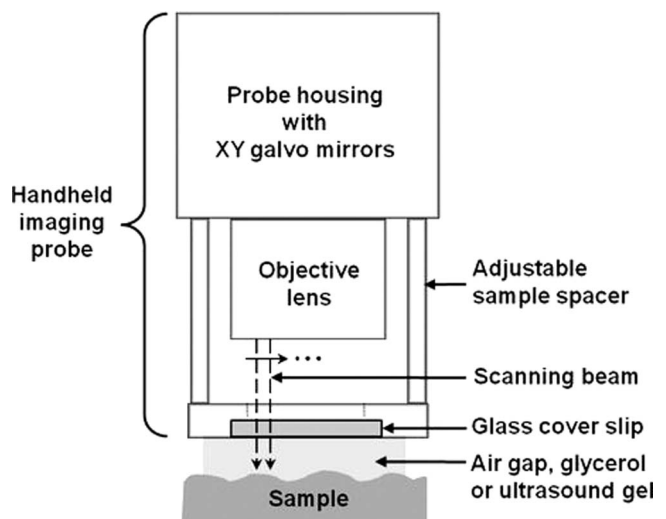


Fig. 2 OCT handheld probe assembly and imaging setup.

embedded within it. The optical fibers provide known features to enable the assessment of distortion. This bed of fibers was located at a depth of $448 \pm 12 \mu\text{m}$ and the fibers were aligned in parallel at $340 \pm 40 \mu\text{m}$ spacing. The phantom has a nominal overall thickness of $630 \mu\text{m}$. The fabrication process was similar to that used for the first phantom, with the exception that the manually prealigned series of fibers was placed in the mold before adding the TiO_2 /silicone mixture. We refer to this phantom as the morphology phantom.

For both phantoms, 3D scans were acquired for three different media present in the $350 \pm 50 \mu\text{m}$ gap between the glass cover slip and the sample: air, glycerol (99.5%) and ultrasound gel (Fig. 2). The handheld probe was mounted on a stationary platform and the beam focus was positioned at $600 \pm 50 \mu\text{m}$ below the sample surface. The samples were affixed across the hole of a mirror mount. The group RI of the phantom, glycerol, and ultrasound gel was measured according to the method described by Tearney et al.³² at a wavelength of 1325 nm and at room temperature of $25 \pm 1^\circ\text{C}$.

2.2.2 Human subject study

Ten human volunteers (5 males, 5 females, mean age: 28 years) were enrolled in this study. Informed consent was obtained prior to the study. A location on the ventral forearm skin of each volunteer was marked with a waterproof marker. The skin was scanned under the same conditions and settings described in the phantom study except that the probe was held manually in position during scanning. Imaging with an air gap was carried out in non-contact mode between the glass cover slip and the skin, whereby the spacing between the glass cover slip and the skin surface was created with a ring (not shown). The ring was removed during scanning when an RI-matching medium was used. The spacing between the glass cover slip and the skin surface was created by ensuring a layer of the medium was present. The skin surface furrows were preserved during the scanning process by placing the probe on the skin with minimal pressure such that the layer was not unduly reduced in thickness.

To assess the effect of an RI-matching medium on epidermal thickness, the scans were performed before application of a medium, and at different time-points after their application (within 30 s, and at 5, 10, 15, 20, 25, 30, and 60 min). Between scanning with different media at the same location, the skin was cleaned with water, dried, and 3 h were allowed to elapse to ensure recovery from any modification caused by the medium. Complete recovery was confirmed by a measured epidermal thickness within 1% of the baseline value on each subject prior to the application of each medium.

2.3 Data Analysis

2.3.1 Quantification of reduction in morphological artifacts

The morphology phantom, with optical fibers at known positions, was used to quantify the reduction in morphological artifact after the application of different RI-matching media. This quantification was not performed on the skin images of human subjects, as there was no available means of independent corroboration of the subsurface features.

Three 3D data sets were acquired with air, glycerol, or ultrasound gel, respectively, at the phantom interface. Fifty equally spaced B-scans were selected from each and the fiber cross sections were manually segmented using a segmentation tool developed in MATLAB (vR2007a, Mathworks, Natick, Massachusetts). Recall that half of the surface of this phantom was flat, and the other half was a positive replica of human ventral forearm skin. Optical fibers under the flat surface were taken as controls, and fibers under the skin replica were used to assess the impact of different RI-matching media. Thus, we assessed four categories of segmented fibers, with total numbers of each in brackets, as follows: i. Control (733); ii. Air (348); iii. Glycerol (344); and iv. Ultrasound gel (338). Fiber cross sections masked by shadows of highly scattering/reflectance structures above them were excluded from the analysis.

Since the undistorted cross section of a control fiber is elongated in the OCT image (due to the higher RI of the fiber compared to air), ellipses were fitted to these segmented cross sections by varying their major axis length, minor axis length, and orientation. Orientation was included in the exhaustive fitting process as the fibers were found to be slightly misoriented with a small angle between their long axis and the scanning plane. Distortion in the shape of the cross section of each optical fiber was quantified using the Dice coefficient,^{33,34} which is a normalized measure of the overlap between the cross sections of a segmented optical fiber and an ideal ellipse. Dice coefficient scores lie in the range 0 to 1, with larger scores indicating a greater overlap and a score of 1 indicating a perfectly elliptical cross section. We report the median and interquartile range of Dice coefficients for each of the four categories. The median is reported instead of the mean because the distribution of data was found to be slightly skewed.³⁵

2.3.2 Quantification of reduction in intensity artifacts

Intensity artifacts characteristically present as low-intensity vertical streaks originating under the skin furrows, indicating a reduction in the power of backscattered light detected from these locations. To quantify this, we estimated the relative change in signal power at the region under skin furrows to that of the adjacent artifact-free region before and after the application of either glycerol or ultrasound gel.

Incident power on a skin region was calculated by integrating the power within a window of A-scans (in linear signal intensity scale) over a range of depths from the skin surface (excluding surface reflections) to a depth of 1.5 mm. The window width of $25 \mu\text{m}$, which corresponds to 5 A-scans, was empirically chosen as matching the typical width of the intensity artifacts. Skin regions containing shadows caused by air bubbles within the RI-matching medium were excluded from the analysis.

The ratio of the detected power in the region under a furrow to that of an adjacent artifact-free region was calculated for the three different interfacing conditions. To estimate the variation in the measured power ratio in such adjacent artifact-free regions, a control (i.e., a second artifact-free region adjacent to the furrow) was selected and its power ratio estimated. Median and interquartile range of the power ratio of a total of 500 collocated skin furrows (i.e., 50 per subject for 10 subjects) and 500 controls were quantified for each RI-matching medium and for air.

2.3.3 Measurement of epidermal thickness

Using 3D OCT data sets of *in vivo* human skin, a collocated B-scan (taken at approximately the same lateral position) was manually selected for analysis from the 3D image set at each time point as described in Sec. 2.2.2. Determination of the epidermal thickness was carried out using a manual distance measurement tool developed in MATLAB (vR2007a, Mathworks, Natick, Massachusetts).

An OCT image of thin human skin consists primarily of two layers, the epidermis and dermis. We estimated epidermal thickness as the distance between the surface reflection and the first well-demarcated transition in reflectance intensity, i.e., from the lower backscatter of the epidermis to the higher backscatter of the dermis. Ten length measurements were carried out per image at five selected ridges and five furrows. These measurements were corrected assuming an average group RI of skin of 1.43 (Ref. 27) at 1325 nm and their mean was calculated. Although it is known that the RI of skin varies in the second decimal place,³⁶ this choice of RI was made to enable convenience of comparison with previous results (i.e., Ref. 27). Percent thickening of the epidermis with time was calculated relative to the baseline epidermal thickness measurement. To minimize intra-operator variation, all measurements were performed by a single investigator.

2.3.4 Statistical analysis

Statistical analysis was used to establish the efficacy of each medium. The extent of the reduction of morphological and intensity distortions was compared using the Welch F-test and a *post hoc* Games–Howell test with the significance level set at $\alpha = 0.05$. Changes in epidermal thickness were compared using analysis of variance with the significance level set at $\alpha = 0.05$. The analysis was performed with the Statistical Package for Social Sciences (SPSS, v16.0, IBM Corporation, Somers, New York).

3 Results

3.1 Skin phantom study

Figure 3 illustrates the effects of glycerol and ultrasound gel on intensity artifacts in the intensity phantom. The dark lines visible below the skin surface in the *en face* images [Rows 1 to 3 of Fig. 3(a)] replicate the topography of the surface furrows. These lines arise from dark vertical streaks in the B-scans, which emerge under skin furrows, as shown in the last row. When glycerol or ultrasound gel is used, these streaks are reduced in magnitude and commence at a greater depth.

OCT images of the morphology phantom, acquired with the three different media, are shown in Fig. 4. For each medium, a set of 3D rendered images and two-dimensional cross-sections are shown. Morphological artifacts are evident under skin furrows, but are absent in regions under flat surfaces. Overall, the artifacts are much more pronounced for the case of an air interface. The bottom surface of the phantom was exposed to air during imaging. This resulted in full-depth vertical white streaks caused by strong bottom surface reflections at some locations evident in the B-scan images in Fig. 4, but these did not significantly affect the analysis.

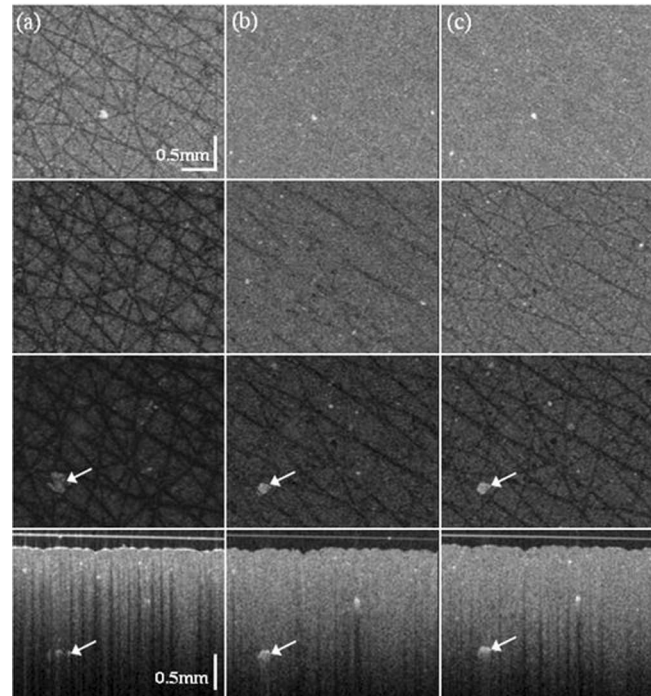


Fig. 3 OCT images of the intensity phantom designed to demonstrate intensity artifacts. Images obtained with: (a) air, (b) glycerol, and (c) ultrasound gel interfaces. The top three rows show *en face* images of the phantom at depths (uncorrected for RI) of 0.5, 1.0, and 1.5 mm from the surface, respectively; the bottom row shows typical vertical cross-sectional images of the phantom. The arrows highlight the same aggregation of TiO₂ scatterers in the phantom; vertical scale bar is not corrected for RI.

Figure 4(a) demonstrates morphological distortion of the regularly spaced array of single-mode fibers embedded within the phantom for the case of an air interface. Visually, the circular cross sections of the optical fibers are broadened, thinned, or almost undetectable (labeled with solid arrows in CS1). These distortions are indicated by a lower Dice coefficient of 0.85 compared to that of the control 0.95 ($p < 0.05$) (Table 1, medium: air). In addition, the long axis (or transverse cross sections) of the fibers appeared furrowed (or bent) and truncated at some points (labeled with a solid arrow in CS2). This furrowed appearance of the fiber's long axis mirrors the shape of surface furrows, but on a reduced scale (due to the relative change in RI and ratios of air and phantom in the beam path). Similar distortions were also observed to affect the base surface of the phantom (labeled with dotted arrows in CS1 and CS2). The intensity artifacts seen in Fig. 3 could also be observed under the surface furrows in Fig. 4(a).

The application of RI-matching media is seen to effectively reduce these artifacts [Figs. 4(b) and 4(c)]. Under the surface furrows, both the cross sections and long axes of the fibers, as well as the bottom surface of the phantom, appear much less distorted [labeled by solid and dotted arrows in Figs. 4(b) and 4(c)]. The results in Table 1 show that use of either glycerol or ultrasound gel has decreased these morphological distortions by significantly increasing the Dice coefficient to 0.95 ($p < 0.05$), which is comparable to that of the control fibers (i.e., 0.96).

The mean group RI of the phantom, glycerol, and ultrasound gel was determined to be 1.41 ± 0.02 , 1.47 ± 0.01 , and

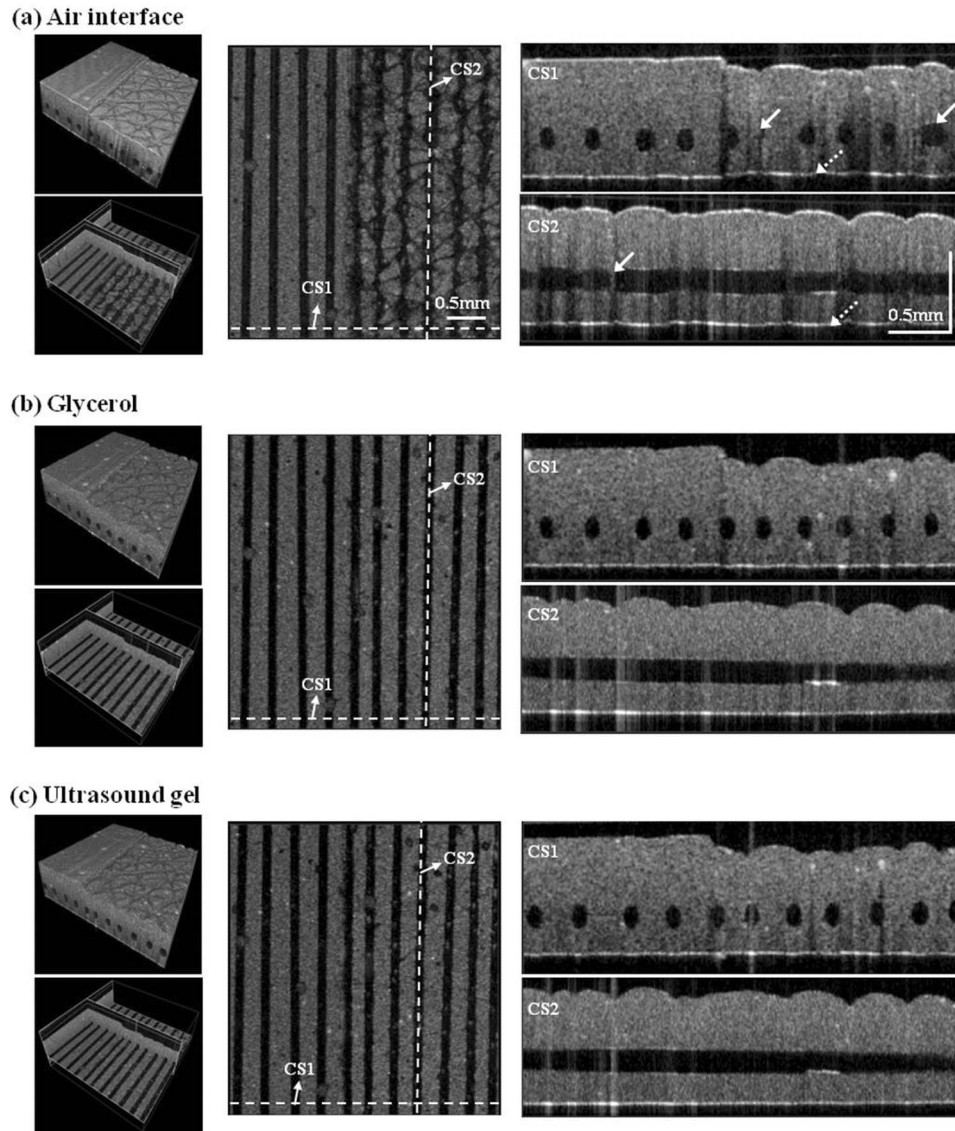


Fig. 4 OCT images of the morphological phantom containing fibers designed to demonstrate morphological artifacts. For each of (a), (b), and (c): Upper left: 3D solid rendering of the phantom; Lower left: orthogonal cut-away views of the phantom; Middle: *en face* image of the phantom at the level through horizontal midline of the fibers' cross-sections; Upper and lower right: vertical cross-sectional images CS1 and CS2, respectively, as indicated in *en face* image. Vertical scale bar is not corrected for RI.

1.34 ± 0.01 , respectively. The RI of glycerol is higher than that of the phantom and the RI of ultrasound gel is lower, although both media have comparable mismatches (0.06 and 0.07, respectively) with the phantom. Glycerol and ultrasound gel showed subtle differences in reducing the intensity artifacts but statistically the same ($p > 0.05$) efficacy in minimizing the morphological artifacts. We observed that the intensity streaks were seen to commence at a greater depth by approximately 10% when using glycerol than when using ultrasound gel.

3.2 Human Subject Study

For *in vivo* scans of human skin, a reduction was observed in the level of both intensity and morphological artifacts after the application of glycerol or ultrasound gel. Figure 5 shows the *en face* images of human ventral forearm skin at 0.5 and 1 mm

below the skin's surface. As with the phantom data (Fig. 4), the onset of the intensity streaks was seen to occur at a greater depth after application of the media. These streaks, however, are less pronounced in the skin after RI matching. Note that air bubbles trapped within the RI-matching medium (labeled with arrows) can significantly attenuate the image intensity beneath the bubble.

Figure 6 shows two examples of artifact-containing B-scans of human ventral forearm skin containing blood vessels (labeled B) and hair follicles (labeled H) under the three interface conditions. In each example, images are approximately collocated. RI matching has reduced the intensity of surface reflections, and increased the useful penetration depth (from ~ 1 mm with air, to ~ 1.5 mm with glycerol or ultrasound gel). In the image obtained with an air interface, dark streaks (labeled with dotted arrows) partially obscure the blood vessels and hair follicles.

Table 1 Quantification results of image artifacts and epidermal thickness.

| Parameter | Quantification metric and statistical measure | Medium | Results |
|------------------------|--------------------------------------------------|----------------|--------------------------|
| Morphological artifact | Dice coefficient: Median (IQR) ^a | Control | 0.96 (0.95 to 0.96) |
| | | Air | 0.85 (0.75 to 0.90) |
| | | Glycerol | 0.95 (0.94 to 0.96) |
| | | Ultrasound gel | 0.95 (0.94 to 0.96) |
| Intensity artifact | Power ratio: Median (IQR) | Control | 1.00 (0.92 to 1.09) |
| | | Air | 0.44 (0.33 to 0.59) |
| | | Glycerol | 1.02 (0.91 to 1.16) |
| | | Ultrasound gel | 1.01 (0.91 to 1.13) |
| Epidermal thickness | Percent changes, %: Mean (\pm standard error) | Air | 5 min : 0 |
| | | | 20 min : 0 |
| | | Glycerol | 5 min : 8 (\pm 0.5) |
| | | | 20 min : 11 (\pm 0.9) |
| | | Ultrasound gel | 5 min : 9 (\pm 1.0) |
| | | | 20 min : 14 (\pm 0.9) |

^aIQR – interquartile range.

The blood vessels are also distorted in shape, i.e., truncated and bent (labeled with solid arrows), corresponding to the morphological artifact described for the phantom. Both these effects are reduced after application of either medium.

Quantitative analysis (Table 1) shows that, with an air interface, the region under a skin furrow contained only 0.44 of the signal power present in the adjacent artifact-free region. Glycerol and ultrasound were found to minimize intensity artifacts,

with power ratio of 1.02 and 1.01, respectively. This is comparable to the power ratios measured in the control regions of 1.0. The median power ratio is not expected to be exactly 1 as it is calculated from A-scans in different regions, albeit adjacent regions, of the skin. Both glycerol and ultrasound gel show comparable reduction in image artifacts and the difference between the two are not significant ($p > 0.05$).

Figure 7 shows the average percentage thickening of epidermis versus time for 10 subjects after the application of either medium. Both media cause an increase in the epidermal thickness by 5% to 6% within 30 s of application. The increase in epidermal thickness plateaued at \sim 20 min and remained unchanged after 1 h. At 20 min, both glycerol and ultrasound gel had significantly thickened the epidermis, by 14% and 11%, respectively.

Table 1 summarizes the quantitative results on image artifacts and epidermal thickness.

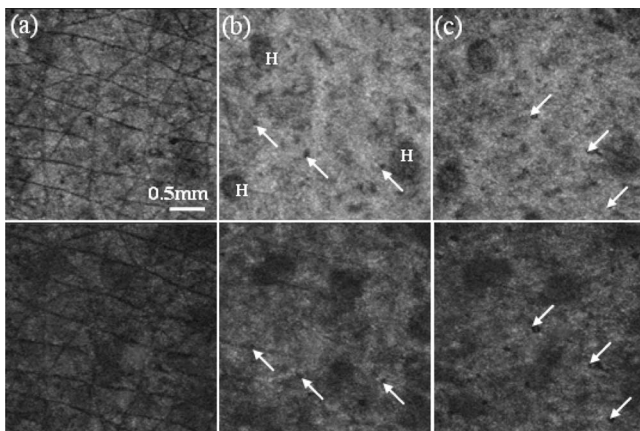


Fig. 5 *En face* OCT images of human ventral forearm skin at 0.5 mm (top row) and 1 mm (bottom row) (uncorrected for RI) below the skin's surface, obtained with: (a) air; (b) glycerol; and (c) ultrasound gel interfaces. Arrows highlight shadow artifacts caused by trapped air bubbles within the RI-matching medium. H: Hair follicle.

4 Discussion

The results presented here demonstrate the severity of intensity and morphological artifacts in OCT images of skin. Although we did not have access to gold standard histology, *a priori* knowledge of skin structures, combined with comparison of images recorded using different media and quantification has enabled us to draw a number of useful conclusions discussed below. These artifacts appear most prominently under skin furrows and are a function of the marked change in RI between tissue and air. The use of glycerol or ultrasound gel was shown to reduce these

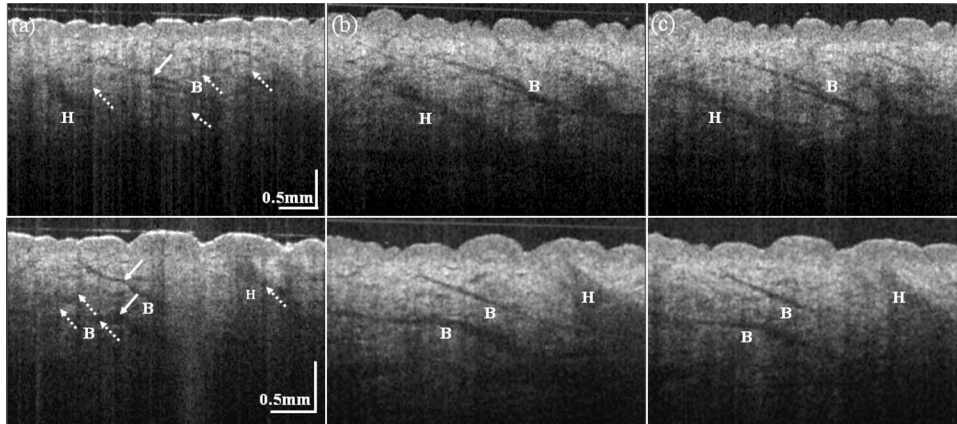


Fig. 6 Two examples of OCT vertical cross-sectional images (B-scans) of human ventral forearm skin. Images were acquired using: (a) air; (b) glycerol; and (c) ultrasound gel interfaces. B: blood vessels; H: hair follicles; vertical scale bar is not corrected for RI.

artifacts by reducing the RI-mismatch at the air-skin interface. The qualitative and quantitative assessment presented here has shown no significant difference, with regard to these artifacts, in the use of either medium for *in vivo* human skin imaging.

Both types of image artifacts in OCT have been shown to be detrimental to the correct interpretation and quantification of subsurface structures of the skin. The shape of blood vessels can be obscured by the dark streaks and can appear distorted. It seems likely that smaller features may be completely occluded. Support for this assertion is contained in Fig. 8, which shows a 3D projection image of a skin phantom containing a large collection of small scattering objects (aggregates of titanium dioxide particles). Many of these objects are undetectable in the air-interfaced phantom, but are visible after the application of either medium.

The low-numerical aperture focusing optics in the sample arm limits the lateral extent of the illumination and collection of light, thus, discriminating in favor of the detection of backscattered/reflected light from the sample focal volume and suppressing signal outside this volume.^{1,37} We hypothesize that the uneven surface of the skin, especially the skin furrows, causes

rapid divergence or deflection of the incident beam. Since at the skin surface the furrow dimensions typically exceed those of the beam, the beam location in relation to the furrow determines the relative importance of divergence or deflection. The net effect, though, of either effect is a reduction in the signal intensity in the region beneath the skin furrows (i.e., an intensity artifact presenting as a low-intensity streak). In the *in vivo* human skin images shown in Fig. 5, RI matching is shown to reduce the signal loss and to delay the onset of these intensity artifacts to ~ 1 mm in physical distance below the surface.

OCT produces an image based on the assumption that light has propagated along a straight beam path. However, when the light beam is deflected off-axis by the furrowed skin surface, the result is displacement of all or part of a feature laterally. The morphological distortions shown in Fig. 4(a) illustrate this. The broadening or thinning of the irregular and variable cross sections of the single-mode fibers embedded under the skin-textured portion of the morphology phantom is largely absent for the fibers under the flat portion.

OCT generates images in which the depth coordinate is based on the optical path length, not the physical path length. The morphological distortions caused by optical path length changes are illustrated in Fig. 9, which shows OCT vertical cross-sectional images of a phantom similar to the phantom that produced the images shown in Fig. 4, except that its surface is flat. The changes in optical path length cause features to appear stretched, as shown by the elongation (in height) of the circular cross sections of the fibers and the phantom (Fig. 9, top row). Changes in the optical path length occurring when the proportions of the sample and air vary can also cause displacement and truncation of a feature vertically relative to the adjacent sections. This is demonstrated in Fig. 9(b) (top row), in which the positions of adjacent fibers are shifted vertically, and the fiber's cross section below the edge is truncated (as labeled) due to a difference in the thickness of the layer above these fibers and the difference in RI between the phantom and air. Similar distortion can be observed for *in vivo* human skin in Fig. 6(a), in which an abrupt change in the thickness of the epidermis has caused displacement in the image of portions of a blood vessel.

Correction of such morphological distortions caused exclusively by changes in the optical path length can be performed by

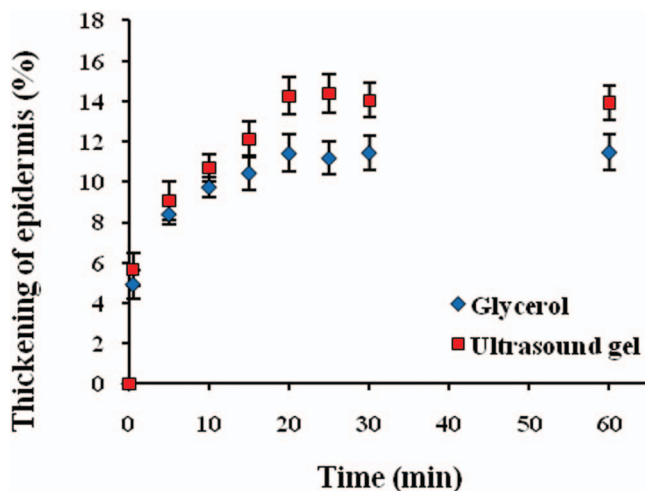


Fig. 7 Average percentage thickening of epidermis after the application of glycerol or ultrasound gel. Error bars represent standard error.

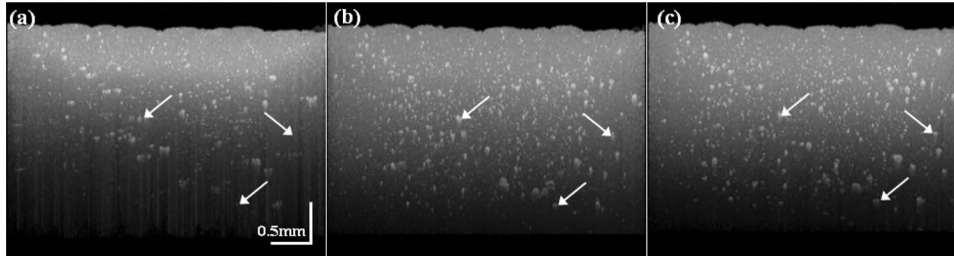


Fig. 8 Three-dimensional projection of a 3D clear render (i.e., background of the scattering structures was made transparent) of the intensity-distortion phantom images shown previously in Fig. 3 acquired with: (a) air; (b) glycerol; and (c) ultrasound gel interfaces. Arrows indicate examples of small scatterers (aggregates of titanium dioxide particles) occluded in (a); vertical scale bar is not corrected for RI.

scaling or shifting the pixel location of the sample as a function of sample's RI, assuming it is known. In practice, this simply requires scaling the path length for each tissue type (or air) by the RI, as we have done in Fig. 9 (bottom row). This procedure accounts for differences between the optical and physical path length. However, it does not account for feature displacement in 3D arising from beam deflection caused by the irregular shape of skin-furrows.

Improvement in penetration depth/transmittance of skin by both glycerol and ultrasound gel were observed (Fig. 6) in this study. This is consistent with previous reports on the use of optical immersion agents such as glycerol, glycerol-water solutions, and ultrasound gel.³⁸⁻⁴¹ Several mechanisms have been proposed to explain this optical clearing effect. These include reduction in optical scattering due to matching of refractive indices of tissue scatterers (keratinocyte components in the epidermis, and collagen and elastin fibers in the dermis) with interstitial fluids;^{42,43} dehydration of excised tissue samples;⁴³⁻⁴⁵ and dissociation⁴⁶ and structural modifications⁴⁰ of collagen fibers.

While this increased image penetration depth observed with glycerol and ultrasound gel is positive, their use was also observed to significantly thicken the epidermis (Fig. 7). This is undesirable in situations where measurement of the epidermal thickness is of clinical significance. The thickening (5% to 6%) of the skin we observed in the first 30 s after application of the medium is most likely to be due to optical changes rather than a physiological effect, as the diffusion of a medium through skin normally takes minutes³⁹ or hours.⁴² It is reasonable to expect that within the first minute, the stratum corneum, which is

composed of dead and loosely connected keratinocytes, is likely to be permeated with the glycerol/ultrasound gel, replacing trapped air with the agent, and increasing the optical path length through the epidermis. We have confirmed this in a separate experiment (results not shown) using tape stripping to remove the stratum corneum prior to the application of the media. In this case, rapid increase in epidermal thickness is absent, although the same value is attained after 1 h. Tape stripping, however, is not feasible in many clinical measurement scenarios of interest.

As glycerol is a hydrophilic humectant (i.e., a water-soluble material with high water absorption capability),⁴⁷ subsequent swelling of the epidermis could be due to the attraction of water from the air or from deeper layers of the skin. It may also be due to the absorption of glycerol by the skin. Genina et al.⁴⁴ have shown that water loss and osmotic agent diffusion into the skin can take place simultaneously through intact stratum corneum albeit at a slower rate than in perforated skin. Ultrasound gel, on the other hand, contains a water-soluble polymer that may be absorbed by the skin.

Since RI-matching media reduce image artifacts, we recommend their use in an OCT skin-imaging protocol when imaging subsurface structures such as microvasculature and hair follicles. Epidermal thickness assessment should be performed without any RI-matching medium. As the efficacy of glycerol and ultrasound gel is comparable in reducing image artifacts, ultrasound gel is preferred for clinical applications as its higher viscosity makes its use more practical, although it is more susceptible to trapped air bubbles.

5 Conclusion

We have shown that the RI-matching media glycerol and ultrasound gel are effective in reducing intensity and morphological artifacts in OCT images of skin-mimicking phantoms and *in vivo* human skin. Both media produced comparable reductions in image artifacts and both led to thickening of the epidermis. Thus, we recommend performing OCT scanning of skin *in vivo* with application of an RI-matching medium for subsurface structure assessment, and without for epidermal thickness assessment.

Acknowledgments

The authors gratefully acknowledge the following colleagues who contributed to this study: Timothy R. Hillman, Andrea Curatolo, Loretta Scolaro, Brendan Kennedy, Blake Klyen, Dirk Lorensen, Rodney Kirk, Xiao Jie Yang, and Rajesh S. Pillai for

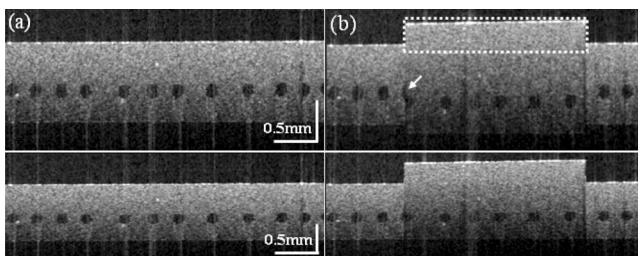


Fig. 9 Morphological distortion caused by optical path length. (a) Top: A silicone phantom embedded with an array of single-mode fibers; Bottom: As above, with vertical scaling by the RI of the phantom. (b) Top: The same phantom as in (a) overlaid with a thin additional layer of similar content (dotted box); Bottom: As above, with vertical scaling by the RI of the phantom. Vertical scale bar for the top row represents uncorrected distance, whereas the bottom row represents corrected distance.

their invaluable suggestions, as well as Nazim Khan from the School of Mathematics and Statistics, UWA, for his help in the statistical analysis. YML has been supported by a scholarship from The University of Western Australia.

References

- D. D. Sampson and T. R. Hillman, "Optical coherence tomography," Chap. 17 in *Lasers and Current Optical Techniques in Biology*, G. Palumbo and R. Pratesi, Eds., pp. 481–571, Royal Society of Chemistry, Cambridge, UK (2004).
- J. Welzel, E. Lankenau, R. Birngruber, and R. Engelhardt, "Optical coherence tomography of the human skin," *J. Am. Acad. Dermatol.* **37**(6), 958–963 (1997).
- R. Steiner, K. Kunzi-Rapp, and K. Scharffetter-Kochanek, "Optical coherence tomography: clinical applications in dermatology," *Med. Laser Appl.* **18**(3), 249–259 (2003).
- T. Gambichler, G. Moussa, P. Regeniter, C. Kasseeck, M. R. Hofmann, F. G. Bechara, M. Sand, P. Altmeyer, and K. Hoffmann, "Validation of optical coherence tomography *in vivo* using cryostat histology," *Phys. Med. Biol.* **52**(5), N75–N85 (2007).
- T. Gambichler, S. Boms, M. Stücker, G. Moussa, A. Kreuter, M. Sand, D. Sand, P. Altmeyer, and K. Hoffmann, "Acute skin alterations following ultraviolet radiation investigated by optical coherence tomography and histology," *Arch. Dermatol. Res.* **297**(5), 218–225 (2005).
- T. Gambichler, B. Künzberger, V. Paech, A. Kreuter, S. Boms, A. Bader, G. Moussa, M. Sand, P. Altmeyer, and K. Hoffmann, "UVA1 and UVB irradiated skin investigated by optical coherence tomography *in vivo*: a preliminary study," *Clin. Exp. Dermatol.* **30**(1), 79–82 (2005).
- B. Querleux, T. Baldeweck, S. Diridollou, J. De Rigal, E. Huguet, F. Leroy, and V. Holloway Barbosa, "Skin from various ethnic origins and aging: an *in vivo* cross-sectional multimodality imaging study," *Skin Res. Technol.* **15**(3), 306–313 (2009).
- J. Welzel, M. Bruhns, and H. H. Wolff, "Optical coherence tomography in contact dermatitis and psoriasis," *Arch. Dermatol. Res.* **295**(2), 50–55 (2003).
- H. Morsy, S. Kamp, L. Thrane, N. Behrendt, B. Saunder, H. Zayan, E. Elmagid, and G. Jemec, "Optical coherence tomography imaging of psoriasis vulgaris: correlation with histology and disease severity," *Arch. Dermatol. Res.* **302**(2), 105–111 (2010).
- N. Scola, A. Goulioumis, and T. Gambichler, "Non-invasive imaging of mid-dermal elastolysis," *Clin. Exp. Dermatol.* **36**(2), 155–160 (2010).
- M. Mogensen, H. A. Morsy, B. M. Nurnberg, and G. B. E. Jemec, "Optical coherence tomography imaging of bullous diseases," *J. Eur. Acad. Dermatol.* **22**(12), 1458–1464 (2008).
- M. Mogensen, L. Thrane, T. M. Joergensen, P. E. Andersen, and G. B. E. Jemec, "Optical coherence tomography for imaging of skin and skin diseases," *Semin. Cutan. Med. Surg.* **28**(3), 196–202 (2009).
- C. Salvini, D. Massi, A. Cappetti, M. Stante, P. Cappugi, P. Fabbri, and P. Carli, "Application of optical coherence tomography in non-invasive characterization of skin vascular lesions," *Skin Res. Technol.* **14**(1), 89–92 (2008).
- M. Mogensen, T. M. Jorgensen, L. Thrane, B. M. Nurnberg, and G. B. E. Jemec, "Improved quality of optical coherence tomography imaging of basal cell carcinomas using speckle reduction," *Exp. Dermatol.* **19**(8), E293–E295 (2010).
- T. Gambichler, P. Regeniter, F. G. Bechara, A. Orlikov, R. Vasa, G. Moussa, M. Stücker, P. Altmeyer, and K. Hoffmann, "Characterization of benign and malignant melanocytic skin lesions using optical coherence tomography *in vivo*," *J. Am. Acad. Dermatol.* **57**(4), 629–637 (2007).
- J. M. Olmedo, K. E. Warschaw, J. M. Schmitt, and D. L. Swanson, "Optical coherence tomography for the characterization of basal cell carcinoma *in vivo*: A pilot study," *J. Am. Acad. Dermatol.* **55**(3), 408–412 (2006).
- S. Zhao, Y. Gu, P. Xue, J. Guo, T. Shen, T. Wang, N. Huang, L. Zhang, H. Qiu, X. Yu, and X. Wei, "Imaging port wine stains by fiber optical coherence tomography," *J. Biomed. Opt.* **15**(3), 036020 (2010).
- J. Ho, D. P. E. Castro, L. C. Castro, Y. Chen, J. Liu, C. Mattox, C. Krishnan, J. G. Fujimoto, J. S. Schuman, and J. S. Duker, "Clinical assessment of mirror artifacts in spectral-domain optical coherence tomography," *Invest. Ophthalmol. Visual Sci.* **51**(7), 3714–3720 (2010).
- S. Ortiz, D. Siedlecki, L. Remon, and S. Marcos, "Optical coherence tomography for quantitative surface topography," *Appl. Opt.* **48**(35), 6708–6715 (2009).
- B. J. Davis, T. S. Ralston, D. L. Marks, S. A. Boppart, and P. S. Carney, "Autocorrelation artifacts in optical coherence tomography and interferometric synthetic aperture microscopy," *Opt. Lett.* **32**(11), 1441–1443 (2007).
- M. J. Everett, K. Schoenenberger, J. B. W. Colston, and L. B. Da Silva, "Birefringence characterization of biological tissue by use of optical coherence tomography," *Opt. Lett.* **23**(3), 228–230 (1998).
- T. Fabritius, S. Makita, Y. Hong, R. Myllylä, and Y. Yasuno, "Automated retinal shadow compensation of optical coherence tomography images," *J. Biomed. Opt.* **14**, 010503 (2009).
- A. Podoleanu, I. Charalambous, L. Plesea, A. Dogariu, and R. Rosen, "Correction of distortions in optical coherence tomography imaging of the eye," *Phys. Med. Biol.* **49**(7), 1277–1294 (2004).
- S. Ricco, M. Chen, H. Ishikawa, G. Wollstein, and J. Schuman, "Correcting motion artifacts in retinal spectral domain optical coherence tomography via image registration," *Medical Image Computing and Computer-Assisted Intervention—MICCAI 2009*, pp. 100–107 (2009).
- J. Welzel, C. Reinhardt, E. Lankenau, C. Winter, and H. H. Wolff, "Changes in function and morphology of normal human skin: evaluation using optical coherence tomography," *Br. J. Dermatol.* **150**(2), 220–225 (2004).
- M. C. Pierce, J. Strasswimmer, B. H. Park, B. Cense, and J. F. de Boer, "Birefringence measurements in human skin using polarization-sensitive optical coherence tomography," *J. Biomed. Opt.* **9**(2), 287–291 (2004).
- T. Gambichler, R. Matip, G. Moussa, P. Altmeyer, and K. Hoffmann, "In vivo data of epidermal thickness evaluated by optical coherence tomography: Effects of age, gender, skin type, and anatomic site," *J. Dermatol. Sci.* **44**(3), 145–152 (2006).
- S. Sakai, M. Yamanari, A. Miyazawa, M. Matsumoto, N. Nakagawa, T. Sugawara, K. Kawabata, T. Yatagai, and Y. Yasuno, "In vivo three-dimensional birefringence analysis shows collagen differences between young and old photo-aged human skin," *J. Invest. Dermatol.* **128**(7), 1641–1647 (2008).
- M. Mogensen, H. A. Morsy, L. Thrane, and G. B. E. Jemec, "Morphology and epidermal thickness of normal skin imaged by optical coherence tomography," *Dermatology* **217**(1), 14–20 (2008).
- V. de Giorgi, M. Stante, D. Massi, L. Mavilia, P. Cappugi, and P. Carli, "Possible histopathologic correlates of dermoscopic features in pigmented melanocytic lesions identified by means of optical coherence tomography," *Exp. Dermatol.* **14**(1), 56–59 (2005).
- M. Mogensen, B. Nürnberg, J. Forman, J. Thomsen, L. Thrane, and G. Jemec, "In vivo thickness measurement of basal cell carcinoma and actinic keratosis with optical coherence tomography and 20-MHz ultrasound," *Br. J. Dermatol.* **160**(5), 1026–1033 (2009).
- G. J. Tearney, M. E. Brezinski, J. F. Southern, B. E. Bouma, M. R. Hee, and J. G. Fujimoto, "Determination of the refractive index of highly scattering human tissue by optical coherence tomography," *Opt. Lett.* **20**(21), 2258–2260 (1995).
- L. R. Dice, "Measures of the amount of ecologic association between species," *Ecology* **26**(3), 297–302 (1945).
- D. W. Shattuck, G. Prasad, M. Mirza, K. L. Narr, and A. W. Toga, "Online resource for validation of brain segmentation methods," *NeuroImage* **45**(2), 431–439 (2009).
- A. McCluskey and A. G. Lalkhen, "Statistics II: Central tendency and spread of data," *Contin. Educ. Anaesth. Crit. Care Pain* **7**(4), 127–130 (2007).
- A. Knüttel and M. Boehlau-Godau, "Spatially confined and temporally resolved refractive index and scattering evaluation in human skin performed with optical coherence tomography," *J. Biomed. Opt.* **5**(1), 83–92 (2000).
- T. G. van Leeuwen, D. J. Faber, and M. C. Aalders, "Measurement of the axial point spread function in scattering media using single-mode fiber-based optical coherence tomography," *IEEE J. Sel. Topics Quantum Electron.* **9**(2), 227–233 (2003).
- V. V. Tuchin, D. A. Zimnyakov, I. L. Maksimova, G. G. Akchurin, A. A. Mishin, S. R. Utz, and I. S. Peretochkin, "Coherent, low-coherent,

- and polarized light interaction with tissues undergoing refractive-index matching control," *Proc. SPIE* **3251**, 12–21 (1998).
39. R. Cicchi, F. S. Pavone, D. Massi, and D. D. Sampson, "Contrast and depth enhancement in two-photon microscopy of human skin *ex vivo* by use of optical clearing agents," *Opt. Express* **13**(7), 2337–2344 (2005).
 40. X. Wen, Z. Mao, Z. Han, and V. V. Tuchin, "In vivo skin optical clearing by glycerol solutions: mechanism," *J. Biophoton.* **3**(12), 44–52 (2010).
 41. Z. Mao, D. Zhu, Y. Hu, X. Wen, and Z. Han, "Influence of alcohols on the optical clearing effect of skin *in vitro*," *J. Biomed. Opt.* **13**(2), 021104 (2008).
 42. V. V. Tuchin, "Optical clearing of skin," Chap. 3 in *Optical Clearing of Tissues and Blood*, pp. 61–82, PM 154, SPIE Press, Bellingham, Washington (2006).
 43. E. A. Genina, A. N. Bashkatov, K. V. Larin, and V. V. Tuchin, "Light-Tissue Interaction at Optical Clearing," Chap. 7 in *Laser Imaging and Manipulation in Cell Biology*, F. S. Pavone, Ed., pp. 115–164, Wiley-VCH Verlag GmbH & Co. KGaA, Weinheim (2010).
 44. E. A. Genina, A. N. Bashkatov, A. A. Korobko, E. A. Zubkova, V. V. Tuchin, I. Yaroslavsky, and G. B. Altshuler, "Optical clearing of human skin: comparative study of permeability and dehydration of intact and photothermally perforated skin," *J. Biomed. Opt.* **13**(2), 021102 (2008).
 45. R. K. Wang, X. Xu, V. V. Tuchin, and J. B. Elder, "Concurrent enhancement of imaging depth and contrast for optical coherence tomography by hyperosmotic agents," *J. Opt. Soc. Am. B* **18**(7), 948–953 (2001).
 46. A. T. Yeh, B. Choi, J. S. Nelson, and B. J. Tromberg, "Reversible dissociation of collagen in tissues," *J. Invest. Dermatol.* **121**(6), 1332–1335 (2003).
 47. L. Baumann, "Moisturizing agents," Chap. 32 in *Cosmetic Dermatology: Principles and Practice*, 2nd ed., pp. 273–277, McGraw-Hill Professional, China (2009).